Three-dimensional response of multilayer FG-GPLRC spherical panels under blast loading

Yasin Heydarpour[1], Parviz Malekzadeh[1*], Hanxing Zhu[2*]

[1]*Department of Mechanical Engineering, School of Engineering, Persian Gulf University, Bushehr 7516913798, Iran*

[2] *School of Engineering, Cardiff University, Cardiff CF24 3AA, UK*

Abstract

In the present research, the dynamic responses of the multilayer functionally graded graphene platelets reinforced composite (FG-GPLRC) spherical panels under blast loading are studied. Three-dimensional elasticity theory is employed to derive the governing equations. The distribution of graphene platelets (GPLs) in each layer is uniform and random with a constant weight fraction. GPLs concentration across the panel thickness may be uniform or graded. The layerwise-differential quadrature method (LW-DQM) together with a non-uniform rational B-spline based multi-step time integration scheme is used to discretize the motion equations. The convergence behavior of the method is examined numerically. Further, to assure its accuracy, the results in the limit cases are compared with those available in the literature. Finally, through the parametric studies, the effects of material and geometrical parameters such as GPLs distribution patterns, GPLs weight fraction and dimension ratios on the transient responses of the FG-GPLRC spherical panels subjected to blast loading are investigated.

Keywords: Dynamic response; Layerwise-differential quadrature method; Graphene platelets reinforced composite; Functionally graded; Spherical panels.

* Corresponding author. Tel.: +98 77 31222150; fax: +98 77 33440376
E-mail addresses: malekzadeh@pgu.ac.ir; p_malekz@yahoo.com (Parviz Malekzadeh).

* Corresponding author. Tel.: +44 (0) 29 2087 4824
E-mail addresses: zhuh3@cardiff.ac.uk (Hanxing Zhu).

1. Introduction

Spherical panels are important and useful structural elements in many different practical engineering fields such as aerospace crafts, naval vehicles, petroleum and nuclear engineering. These applications of spherical panels in different industries demand that the heterogeneity of the materials should be considered in the response analysis of the panels. Hence, research on high performance materials to improve their structural behavior, chemical protection against corrosion and wear, fatigue life, and their other physical properties is an essential task. The importance of the subject is the main motivation for detailed investigation of this study.

Graphene platelets reinforced composites (GPLRCs) are a relatively new class of composite materials with many different exceptional properties[1,2]. In this type of materials, usually an isotropic polymer matrix is reinforced with uniformly distributed, randomly oriented and rectangular shaped graphene platelets (GPLs). The main advantages of GPLs over the conventional reinforcement materials are their lighter weight and higher strength and stiffness [1,2]. In order to use the GPLs efficiently, it is preferred to scatter them in the polymer matrix with a graded distribution. Due to practical limitation in continuously changing their volume fraction, a layerwise approach has been suggested [3-5]. Accordingly, the discrete GPLRC layers are bonded together to construct nanocomposites with the desired properties. In this approach, the GPLs are assumed to be uniformly distributed in each layer with random orientation. To ensure that the nanocomposite material properties have no abrupt change in the thickness direction, the volume fractions of GPLs in two adjacent layers have no obvious difference. These functionally graded GPLRC (FG-GPLRC) materials have recently gained considerable research attention in the engineering community [6]. As an important step in the design and manufacturing operations of

FG-GPLRC spherical panels, it is crucial to investigate their transient response under blast loading.

In the recent years, there has been an increasing amount of literature on the dynamic and static analyses of isotropic, functionally graded and laminated composite shells and plates; see for example Refs. [7-26]. Many studies have been focused on the free vibration behaviors, dynamic and thermoelastic analyses of different FG-GPLRC structures such as beams, plates, panels, cylindrical and conical shells in recent years [27-44]. However, to the best of our knowledge, less attention is devoted to the mechanical and thermo-mechanical behavior of FG- GPLRC spherical panels [41-48]. In addition, the nonlinear vibration of shell-type structures and the buckling of microbeams and microtubes under different conditions have been investigated by some researchers in recent years; see for example Refs. [49-55].

Heydarpour et al. [41] studied the transient thermoelastic behaviors of complete FG-GPLRC spherical shells under thermo-mechanical loadings based on the Lord-Shulman thermoelasticity theory. Eyvazian et al. [42] analyzed the free vibration characteristics of FG-GPLRC spherical shells on elastic foundation in the context of the first-order shear deformation theory (FSDT) of shells. They utilized the generalized differential quadrature method (GDQM) to discretize the governing equations. The bending and free vibration behaviors of FG-GPLRC cylindrical and spherical panels were investigated by Do and Lee [43] using the higher-order shear deformation theory (HSDT) of shells. Their numerical model was developed based on the isogeometric analysis (IGA). Liu et al. [44] examined the three-dimensional free vibration and bending behaviors of FG-GPLRC spherical shells analytically. In addition, some researchers investigated the vibrational behaviors of FG-GPLRC doubly curved panels. Wang et al. [45] studied the free vibration and static bending of the simply supported FG-GPLRC doubly-curved shallow shells in accordance with the HSDT of shells. Bidzard et al. [46] developed an FSDT based finite element

model for the free vibration of FG-GPLRC toroidal panels. Wang et al. [47] investigated the nonlinear transient response of FG-GPLRC doubly curved shallow shells subjected to blast loads considering thermal effects. They derived the motion equations based on the HSDT of shells under von Kármán geometric nonlinear assumptions. The influences of thermal environment and internal pressure on the nonlinear vibrational behaviors of multilayer FG-GPLRC toroidal panels were studied numerically by Bidzard et al. [48]. They analyzed the panels on a nonlinear elastic foundation with elastic restraints against rotation edges using the finite element method.

The literature survey reveals that the three-dimensional dynamic response of multilayer FG-GPLRC spherical panels subjected to blast loading has not been investigated yet. This research is essential for an accurate evaluation of their structural behaviors and is likely to fill a gap in the state of the art of this problem. The spherical panels under consideration are composed of several GPLs reinforced composite layers. Each of the individual layers is made of an isotropic polymer matrix reinforced with uniformly distributed and randomly oriented GPLs. The numerical solution method is developed using the layerwise differential quadrature method [39,41,56-58] in conjunction with the NURBS based multi-step time integration technique [59,60]. The approach is validated by showing its good convergence rate and performing comparison studies with relevant cases available in the literature. This research work is completed by illustrating the influences of the distribution patterns, weight fraction and geometric parameters of GPLs, and the geometric parameters of the multilayer FG-GPLRC spherical panels on their dynamic behaviors.

2. Governing equations

Fig. 1 (a) shows a typical multilayer FG-GPLRC spherical panel with thickness h, inner radius R_i, outer radius R_o, circumferential and meridian opening angles θ_0 and ϕ_0, respectively. The material points of the panel in the undeformed configuration are identified by using a spherical

coordinate system with coordinate variables (r,θ,φ) (see Fig. 1 (a)). As depicted in Fig. 1 (b), the spherical panel is composed of N_L perfectly bonded concentric GPLRC spherical panel layers. The basic formulation and solution procedure are presented in the following sections.

2.1 GPLRC spherical panel material properties

In producing the multilayer FG-GPLRC shells, the GPLRC shell layers with slightly different GPLs weight fractions are bonded together. Each of the individual spherical panel layers is composed of an isotropic polymer as the matrix phase and rectangular shaped GPLs as the nanofillers reinforcement. The randomly oriented GPLs are uniformly dispersed in the matrix phase of the panel layers. In this approach, the desired functionally graded material properties across the shell thickness are achieved by suitably arranging the GPLRC shell layers. The equivalent Young's moduli of GPLRC panel layers are estimated using the modified Halpin-Tsai micromechanical model. Accordingly, the effective Young's modulus of the e^{th} layer $\left(E^e\right)$ is obtained as [3-5]

$$E^e=\left(\frac{3}{8}\frac{1+\zeta_L\eta_L V_{GPL}^e}{1-\eta_L V_{GPL}^e}+\frac{5}{8}\frac{1+\zeta_T\eta_T V_{GPL}^e}{1-\eta_T V_{GPL}^e}\right)E_m \qquad \text{for } e=1,2,3,\ldots,N_L \tag{1}$$

where E_m and V_{GPL}^e are the matrix Young's modulus and the GPLs volume fraction of the e^{th} layer, respectively. The scaling parameters ζ_L, ζ_T, η_L and η_T depend on the dimensions and material properties of the GPLs, respectively, and are given as

$$\zeta_L=2\left(a_{GPL}/t_{GPL}\right)=\zeta_T\left(a_{GPL}/b_{GPL}\right),\quad \zeta_T=2\left(b_{GPL}/t_{GPL}\right),\quad \eta_L=\frac{\left(E_{GPL}/E_m\right)-1}{\left(E_{GPL}/E_m\right)+\zeta_L},$$

$$\eta_T=\frac{\left(E_{GPL}/E_m\right)-1}{\left(E_{GPL}/E_m\right)+\zeta_T} \tag{2a-d}$$

where a_{GPL}, b_{GPL}, t_{GPL} and E_{GPL} are, respectively, the length, width, thickness and Young's modulus of GPLs. Also, the indices GPL and m correspond to the GPLs and matrix materials,

respectively. The effective mass density ρ^e and Poisson's ratio ν^e of the e^{th} panel layer are determined according to the rule of mixture [5] as follows:

$$\rho^e = \rho_m V_m^e + \rho_{GPL} V_{GPL}^e \tag{3}$$

$$\nu^e = \nu_m V_m^e + \nu_{GPL} V_{GPL}^e \tag{4}$$

where the GPLs and matrix volume fractions are obtained from the following equations,

$$V_{GPL}^e = \frac{w_{GPL}^e}{w_{GPL}^e + \left(\rho_{GPL}/\rho_m\right)\left(1 - w_{GPL}^e\right)}, \quad V_{GPL}^e + V_m^e = 1 \tag{5a,b}$$

and w_{GPL}^e is the GPLs weight fraction of the e^{th} GPLRC spherical panel layer.

The four different GPLs distribution patterns along the thickness have usually been considered in the literature for the FG-GPLRC structural elements such as beams, plates and shells. In the simplest one, the GPLs weight fractions are the same in all the GPLRC shell layers, and the result is a nanocomposite with uniformly distributed (UD) GPLs through the spherical panel thickness. In two other cases, the GPLRC panel layers are so arranged that the GPLs have nonuniform distribution through the shell thickness but mid-plane symmetry. In one of these two cases, both the outer and inner surfaces are GPLs rich (FG-X type) whereas in the other case, the middle surface is GPLs rich (FG-O type). In the fourth case, the inner surface is GPLs-rich, whereas the outer surface is GPLs free (FG-V type). The weight fractions of GPLs in the e^{th} GPLRC panel layer of these four configurations are as follows [41]

$$w_{GPL}^e = \begin{cases} W_{GPL} & \text{UD} \\ 4W_{GPL}\left(\dfrac{N_L+1}{2} - \left|e - \dfrac{N_L+1}{2}\right|\right)\Big/\left(N_L+2\right) & \text{O - type} \\ 4W_{GPL}\left(\dfrac{1}{2} + \left|e - \dfrac{N_L+1}{2}\right|\right)\Big/\left(N_L+2\right) & \text{X - type} \\ 2eW_{GPL}/(N_L+1) & \text{V - type} \end{cases} \quad \text{for } e=1,2,3,\ldots,N_L \tag{6}$$

where W_{GPL} is the total GPLs weight fraction.

2.2 Transient thermoelastic analysis

As the polymer matrix is isotropic and the reinforcement GPLs are uniformly distributed and randomly orientated, the elastic properties of the e^{th} layer of the FG-GPLRC spherical panel are isotropic and the effective Young's modulus and Poison's ratio can be determined using the formulas given in the above section. The three-dimensional constitutive relation of the e^{th} layer is given as

$$\begin{Bmatrix} \sigma_{rr}^{e} \\ \sigma_{\theta\theta}^{e} \\ \sigma_{\phi\phi}^{e} \\ \sigma_{r\theta}^{e} \\ \sigma_{\theta\phi}^{e} \\ \sigma_{\phi r}^{e} \end{Bmatrix} = \begin{bmatrix} C_{11}^{e} & C_{12}^{e} & C_{13}^{e} & 0 & 0 & 0 \\ C_{12}^{e} & C_{22}^{e} & C_{23}^{e} & 0 & 0 & 0 \\ C_{13}^{e} & C_{23}^{e} & C_{33}^{e} & 0 & 0 & 0 \\ 0 & 0 & 0 & C_{44}^{e} & 0 & 0 \\ 0 & 0 & 0 & 0 & C_{55}^{e} & 0 \\ 0 & 0 & 0 & 0 & 0 & C_{55}^{e} \end{bmatrix} \begin{Bmatrix} \varepsilon_{rr}^{e} \\ \varepsilon_{\theta\theta}^{e} \\ \varepsilon_{\phi\phi}^{e} \\ 2\varepsilon_{r\theta}^{e} \\ 2\varepsilon_{\theta\phi}^{e} \\ 2\varepsilon_{\phi r}^{e} \end{Bmatrix} \tag{7}$$

where $\sigma_{ij}^{e}\ (i,j=r,\theta,\phi)$ and $\varepsilon_{ij}^{e}\ (i,j=r,\theta,\phi)$ are the stress and strain tensor components at an arbitrary material point of the e^{th} layer; also, $C_{ij}^{e}\ [i,j=1,2,3,4,5,6]$ are the material elastic coefficients of the e^{th} layer of FG-GPLRC spherical panel. According to the three-dimensional linear elasticity theory, the strain-displacement relations for the e^{th} spherical layer are expressed as

$$\varepsilon_{rr}^{e}=\frac{\partial u^{e}}{\partial r},\quad \varepsilon_{\theta\theta}^{e}=\frac{1}{r}\frac{\partial v^{e}}{\partial\theta}+\frac{u^{e}}{r},\quad \varepsilon_{\phi\phi}^{e}=\frac{1}{r\sin\theta}\frac{\partial w^{e}}{\partial\phi}+\frac{u^{e}}{r}+\frac{v^{e}\cot\theta}{r},\quad \varepsilon_{r\theta}^{e}=\frac{1}{2}\left(\frac{1}{r}\frac{\partial u^{e}}{\partial\theta}+\frac{\partial v^{e}}{\partial r}-\frac{v^{e}}{r}\right),$$
$$\varepsilon_{\theta\phi}^{e}=\frac{1}{2}\left(\frac{1}{r\sin\theta}\frac{\partial u^{e}}{\partial\phi}+\frac{\partial w^{e}}{\partial r}-\frac{w^{e}}{r}\right),\quad \varepsilon_{\phi r}^{e}=\frac{1}{2}\left(\frac{1}{r\sin\theta}\frac{\partial v^{e}}{\partial\phi}+\frac{\partial w^{e}}{r\partial\theta}-\frac{w^{e}\cot\theta}{r}\right) \tag{8a-f}$$

where $u^{(e)}$, $v^{(e)}$ and $w^{(e)}$ are, respectively, the displacement components along the r, θ and ϕ-directions of an arbitrary material point of the e^{th} layer. Also, the material elastic

coefficients C_{ij}^{e} of the e^{th} spherical layer are related to its effective Young's modulus $\left(E^{e}\right)$ and Poisson's ratio $\left(\nu^{e}\right)$ as

$$C_{11}^{e}=C_{22}^{e}=C_{33}^{e}=\frac{\left(1-\nu^{e}\right)E^{e}}{\left(1+\nu^{e}\right)\left(1-2\nu^{e}\right)},C_{12}^{e}=C_{23}^{e}=C_{13}^{e}=\frac{\nu^{e}E^{e}}{\left(1+\nu^{e}\right)\left(1-2\nu^{e}\right)},$$
$$C_{44}^{e}=C_{55}^{e}=C_{66}^{e}=\frac{E^{e}}{2\left(1+\nu^{e}\right)} \tag{9a-c}$$

The motion of the e^{th} layer of FG-GPLRC spherical panel based on the three-dimensional elasticity theory is governed by the following differential equations [61]

$$\frac{\partial\sigma_{rr}^{e}}{\partial r}+\frac{1}{r}\frac{\partial\sigma_{r\theta}^{e}}{\partial\theta}+\frac{1}{r\sin\theta}\frac{\partial\sigma_{r\phi}^{e}}{\partial\phi}+\frac{1}{r}\left(2\sigma_{rr}^{e}-\sigma_{\theta\theta}^{e}-\sigma_{\phi\phi}^{e}+\sigma_{r\theta}^{e}\cot\theta\right)=\rho^{e}\frac{\partial^{2}u^{e}}{\partial t^{2}} \tag{10}$$

$$\frac{\partial\sigma_{r\theta}^{e}}{\partial r}+\frac{1}{r}\frac{\partial\sigma_{\theta\theta}^{e}}{\partial\theta}+\frac{1}{r\sin\theta}\frac{\partial\sigma_{\theta\phi}^{e}}{\partial\phi}+\frac{1}{r}\left[\left(\sigma_{\theta\theta}^{e}-\sigma_{\phi\phi}^{e}\right)\cot\theta+3\sigma_{r\theta}^{e}\right]=\rho^{e}\frac{\partial^{2}v^{e}}{\partial t^{2}} \tag{11}$$

$$\frac{\partial\sigma_{r\phi}^{e}}{\partial r}+\frac{1}{r}\frac{\partial\sigma_{\theta\phi}^{e}}{\partial\theta}+\frac{1}{r\sin\theta}\frac{\partial\sigma_{\phi\phi}^{e}}{\partial\phi}+\frac{1}{r}\left(2\sigma_{\theta\phi}^{e}\cot\theta+3\sigma_{r\phi}^{e}\right)=\rho^{e}\frac{\partial^{2}w^{e}}{\partial t^{2}} \tag{12}$$

where e=1,2,…,N_L and t is the time.

The multilayer FG-GPLRC spherical panel is subjected to a blast loading at its inner surface $\left(r=R_{i}^{1}\right)$ and its outer surface $\left(r=R_{\text{o}}^{N_L}\right)$ is loading free. Thus, the corresponding boundary conditions become

$$\text{At } r=R_{i}^{1}=R_{i}:\ \sigma_{rr}^{1}=-q(t) \tag{13a}$$

$$\text{At } r=R_{\text{o}}^{N_L}=R_{\text{o}}:\ \sigma_{rr}^{N_L}=0 \tag{13b}$$

In Eq. (13a), $q(t)$ is the internal pressure due to blast loading. Also, the external boundary conditions at the edges of the FG-GPLRC spherical panel are classified as

At $\theta=0,\theta_{0}$:

$$\text{Either } u^{e}=0 \quad \text{or} \quad \sigma_{r\theta}^{e}=0 \tag{14a,b}$$

Either $v^e = 0$ or $\sigma^e_{\theta\theta} = 0$ (15a,b)

Either $w^e = 0$ or $\sigma^e_{\theta\phi} = 0$ (16a,b)

At $\phi = 0, \phi_0$:

Either $u^e = 0$ or $\sigma^e_{\phi r} = 0$ (17a,b)

Either $v^e = 0$ or $\sigma^e_{\theta\phi} = 0$ (18a,b)

Either $w^e = 0$ or $\sigma^e_{\phi\phi} = 0$ (19a,b)

The geometric and natural compatibility conditions at the interface of two adjacent GPLRC layers "*e*" and "*e*+1" of the multilayer FG-GPLRC panel require

$$u^e\left(R^e_{\mathrm{o}},t\right) = u^{e+1}\left(R^{e+1}_i,t\right),\ v^e\left(R^e_{\mathrm{o}},t\right) = v^{e+1}\left(R^{e+1}_i,t\right),\ w^e\left(R^e_{\mathrm{o}},t\right) = w^{e+1}\left(R^{e+1}_i,t\right) \quad (20a\text{-}c)$$

$$\sigma^e_{rr}\left(R^e_{\mathrm{o}},t\right) = \sigma^{e+1}_{rr}\left(R^{e+1}_i,t\right),\ \sigma^e_{r\theta}\left(R^e_{\mathrm{o}},t\right) = \sigma^{e+1}_{r\theta}\left(R^{e+1}_i,t\right),\ \sigma^e_{\theta\phi}\left(R^e_{\mathrm{o}},t\right) = \sigma^{e+1}_{\theta\phi}\left(R^{e+1}_i,t\right) \quad (21a\text{-}c)$$

where e=1, 2,…, N_L-1.

It is assumed that the shell is at rest when it is subjected to blast loading, which leads to the following initial conditions

$$u^e\left(r,\theta,\phi,0\right) = 0,\ v^e\left(r,\theta,\phi,0\right) = 0,\ w^e\left(r,\theta,\phi,0\right) = 0,\ \left.\frac{\partial u^e}{\partial t}\right|_{t=0} = 0,\ \left.\frac{\partial v^e}{\partial t}\right|_{t=0} = 0,\ \left.\frac{\partial w^e}{\partial t}\right|_{t=0} = 0 \quad (22a\text{-}f)$$

3. Solution technique

It is obviously not an easy task to obtain closed form analytical solutions for the governing differential equations and to satisfy all the boundary, compatibility and initial conditions. Usually, a suitable accurate approximate method is employed to solve them. In this work, the differential quadrature method (DQM) and a NURBS based multi-step method are applied to discretize the governing equations in the spatial and temporal domains, respectively.

According to the DQM, the e^{th} FG-GPLRC spherical panel layer is discretized into a set of N_r, N_θ and N_ϕ discrete points along the r, θ and ϕ-directions, respectively. To do this, the Gauss–Lobatto–Chebyshev grid generation rule is employed in this study [39,41]. Also, the Lagrange polynomials are considered as the test function to determine the DQ weighting coefficients [39,41]. According to the DQM, the motion equations (i.e. the governing differential equations) are discretized at the domain grid points and are transformed to a system of ordinary differential equations in the temporal domain. Meanwhile, the boundary and compatibility conditions are converted to a system of algebraic equations at the layers boundary grid points.

The differential quadrature (DQ) discretized forms of the motion equations (10)-(12) and the strain-displacement relations (8) for the e^{th} layer are respectively as follows,

$$\sum_{m=1}^{N_r} A_{im}^{r}\left(\sigma_{rr}^{e}\right)_{mjk} + \frac{1}{r_i}\sum_{m=1}^{N_\theta} A_{jm}^{\theta}\left(\sigma_{r\theta}^{e}\right)_{imk} + \frac{1}{r_i \sin\theta_j}\sum_{m=1}^{N_\phi} A_{km}^{\phi}\left(\sigma_{r\phi}^{e}\right)_{ijm} + \frac{1}{r_i}\left(2\sigma_{rr}^{e} - \sigma_{\theta\theta}^{e} - \sigma_{\phi\phi}^{e} + \sigma_{r\theta}^{e}\cot\theta\right)_{ijk}$$
$$= \rho_{ijk}^{e}\frac{d^2 u_{ijk}^{e}}{dt^2} \tag{23}$$

$$\sum_{m=1}^{N_r} A_{im}^{r}\left(\sigma_{r\theta}^{e}\right)_{mjk} + \frac{1}{r_i}\sum_{m=1}^{N_\theta} A_{jm}^{\theta}\left(\sigma_{\theta\theta}^{e}\right)_{imk} + \frac{1}{r_i \sin\theta_j}\sum_{m=1}^{N_\phi} A_{km}^{\phi}\left(\sigma_{\theta\phi}^{e}\right)_{ijm} + \frac{1}{r_i}\left[\left(\sigma_{\theta\theta}^{e} - \sigma_{\phi\phi}^{e}\right)\cot\theta + 3\sigma_{r\theta}^{e}\right]_{ijk}$$
$$= \rho_{ijk}^{e}\frac{d^2 v_{ijk}^{e}}{dt^2} \tag{24}$$

$$\sum_{m=1}^{N_r} A_{im}^{r}\left(\sigma_{r\phi}^{e}\right)_{mjk} + \frac{1}{r_i}\sum_{m=1}^{N_\theta} A_{jm}^{\theta}\left(\sigma_{\theta\phi}^{e}\right)_{imk} + \frac{1}{r_i \sin\theta_j}\sum_{m=1}^{N_\phi} A_{km}^{\phi}\left(\sigma_{\phi\phi}^{e}\right)_{ijm} + \frac{1}{r_i}\left(2\sigma_{\theta\phi}^{e}\cot\theta + 3\sigma_{r\phi}^{e}\right)_{ijk}$$
$$= \rho_{ijk}^{e}\frac{d^2 w_{ijk}^{e}}{dt^2} \tag{25}$$

$$\left(\varepsilon_{rr}^{e}\right)_{ijk} = \sum_{m=1}^{N_r} A_{im}^{r} u_{mjk}^{e}, \left(\varepsilon_{\theta\theta}^{e}\right)_{ijk} = \frac{1}{r_i}\sum_{m=1}^{N_\theta} A_{jm}^{\theta} v_{imk}^{\theta} + \frac{u_{ijk}^{e}}{r_i}, \left(\varepsilon_{\phi\phi}^{e}\right)_{ijk} = \frac{1}{r_i \sin\theta_j}\sum_{m=1}^{N_\phi} A_{km}^{\phi} w_{ijm}^{e} + \frac{1}{r_i}\left(u^{e} + v^{e}\cot\theta\right)_{ijk},$$

$$\left(\varepsilon_{r\theta}^{e}\right)_{ijk} = \frac{1}{2}\left(\frac{1}{r_i}\sum_{m=1}^{N_\theta} A_{jm}^{\theta} u_{imk}^{\theta} + \sum_{m=1}^{N_r} A_{im}^{r} v_{mjk}^{e} - \frac{v_{ijk}^{e}}{r_i}\right), \left(\varepsilon_{\theta\phi}^{e}\right)_{ijk} = \frac{1}{2}\left(\frac{1}{r_i \sin\theta_j}\sum_{m=1}^{N_\phi} A_{km}^{\phi} u_{ijm}^{e} + \sum_{m=1}^{N_r} A_{im}^{r} w_{mjk}^{e} - \frac{w_{ijk}^{e}}{r_i}\right),$$

$$\left(\varepsilon^{e}_{\phi r}\right)_{ijk}=\frac{1}{2}\left(\frac{1}{r_i\sin\theta_j}\sum_{m=1}^{N_\phi}A^{\phi}_{km}v^{e}_{ijm}+\frac{1}{r_i}\sum_{m=1}^{N_\theta}A^{\theta}_{jm}w^{\theta}_{imk}-\frac{w^{e}_{ijk}\cot\theta_j}{r_i}\right) \tag{26a-f}$$

where i=1,2,.., N_r ; j=1,2,.., N_θ ; k=1,2,.., N_ϕ ; A^{α}_{ij} and N_α are the weighting coefficients and numbers of grid point along the α -direction $(\alpha=r,\theta\text{ and }\phi)$. By using the constitutive relation (7), the discretized motion equations (23)-(25) are expressed in terms of the displacement components of the DQ grid points. In a similar manner, the DQ discretized forms of the external boundary conditions, the geometric and natural compatibility conditions at the interface of two adjacent GPLRC layers are obtained. After imposing the boundary conditions, the results become a system of ordinary differential equations (ODEs) in temporal domain, which can be rearranged in the matrix form as

$$[M]\frac{d^2}{dt^2}\{D\}+[K]\{D\}=\{f(t)\} \tag{27}$$

where $[M],[K]$ and $\{f\}$ are the mass matrix, stiffness matrix and load vector, respectively. Also, $\{D\}$ refers to displacement components vector of grid points. Based on the element arrangement of this vector, the elements of the coefficient matrices [M], [K] and the load vector {f} are determined from the discretized form of the governing differential equations and the related boundary and compatibility conditions.

Different time integration techniques can be used to solve the system of the ordinary differential equations (27). A comparatively new one is a multi-step method introduced using the NURBS curves [59,60]. In this study, this new multi-step method is employed to solve the system of differential Eq. (27) subjected to the related initial conditions, as a system of initial value problems. In the first step of this scheme, the system of the second-order ODEs is decomposed into two sets of first-order ones as

$$\begin{cases} \dfrac{d}{dt}\{\eta_1\} = \{\eta_2\} \\ [M]\dfrac{d}{dt}\{\eta_2\} + [K]\{\eta_1\} = \{f(t)\} \end{cases} \tag{28a,b}$$

where $\{\eta_1\} = \{D\}$ and $\{\eta_2\} = \dfrac{d}{dt}\{D\}$. Different multi-step approaches can be developed by using different orders of NURBS curves and also by varying their weighting coefficients (w_i). In the present work, a four-step scheme [60] is adopted with the weighting coefficients $w_1 = 10^{-3}$, $w_2 = 10^{-3}$, $w_3 = 2$ and $w_4 = 3$. According to this scheme, the discretized forms of Eqs. (28a,b) are converted to, respectively,

$$\{\eta_1\}_{n+1} = \{\eta_1\}_n + \Delta t\big(1.50002585\{\eta_2\}_n - 0.5000529\{\eta_2\}_{n-1} + 2.827\times10^{-5}\{\eta_2\}_{n-2} - 1.2\times10^{-6}\{\eta_2\}_{n-3}\big) \tag{29}$$

$$\{\eta_2\}_{n+1} = \{\eta_2\}_n + \Delta t\big(1.50002585\{\hat{\eta}\}_n - 0.5000529\{\hat{\eta}\}_{n-1} + 2.827\times10^{-5}\{\hat{\eta}\}_{n-2} - 1.2\times10^{-6}\{\hat{\eta}\}_{n-3}\big) \tag{30}$$

where Δt is the time step and

$$\{\hat{\eta}\} = [M]^{-1}\big(-[K]\{\eta_1\} + \{f(t)\}\big) \tag{31}$$

As can be seen from the above equations, to start the iteration procedure, the values of the unknown field variables at the first four points must be available. These data at the first point are obtained via the initial conditions. At the next three points, they are determined using the multi-step formulation of the scheme [60]. At the end of iterations, one achieves a system of linear algebraic equations. After performing the multi-step technique, the partial differential governing equations were converted into a set of linear algebraic equations. Consequently, the values of the unknown field variables are evaluated by solving the system of linear algebraic equations at the end of each time step. As can be expected, the results at the end of each iteration are considered as the initial conditions for the next iteration. The outputs of this procedure are the time histories

of the displacement components and the stress components at the DQ grid points of the FG-GPLRC spherical panels.

4. Numerical results

At this stage, firstly, the formulation and solution procedure are validated. After that, the effects of different material and geometric parameters on the transient responses of the FG-GPLRC spherical panels are investigated through the parametric studies. If other values are not specified, a length of $a_{GPL}=2.5(\mu\mathrm{m})$, a width of $b_{GPL}=1.5(\mu\mathrm{m})$ and a thickness of $t_{GPL}=1.5(\mathrm{nm})$ are adopted for the GPLs [39]. Also, the material properties of epoxy (the matrix phase) and GPLs (the reinforcement phase) are presented in Table 1. In the solved examples, eleven GPLRC spherical layers (i.e., $N_L=11$) are used to generate the desired GPLs distribution along the panel thickness. In addition, unless other values are given, the inner and outer radii of the panel are assumed to be $R_i=0.9(\mathrm{m})$ and $R_{\mathrm{o}}=1.1(\mathrm{m})$, respectively. To simplify the interpretation of the results of the FG-GPLRC spherical panels, the following non-dimensional parameters are defined

$$U=\frac{uE_{GPL}h}{{R_m}^2P_0},\quad \xi=\frac{r-R_i}{R_{\mathrm{o}}-R_i},\quad \eta=\frac{\theta}{\theta_0},\quad \mu=\frac{\phi}{\phi_0},\ \Sigma_{ij}=\frac{\sigma_{ij}}{P_0}\ \text{with}\ i,j=r,\theta,\phi \tag{32a-g}$$

where $R_m(=R_i+0.5R_{\mathrm{o}})$ is the mean radius of the FG-GPLRC panel and P_0 is the maximum internal pressure. The transient internal pressure on the inner surface of the panel due to blast loading is simulated as

$$q(t)=P_0e^{-\gamma t}H(t) \tag{33}$$

where $H(t)$ is the Heavyside step function and $\gamma=330\left(\mathrm{s}^{-1}\right)$ [62].

The superiority of the novel NURBS based multi-step scheme over the Newmark algorithm is shown numerically in Table 2. In this table, the convergence rates and the CPU times of both schemes in determining the transient radial displacement of a multilayer FG-GPLRC spherical panel under blast loading are compared. It is observed that the converged results of the two approaches are in close agreement, however, it is obvious that the CPU time requirement of the NURBS based multi-step technique is considerably less than that of the Newmark one. In addition, the results of the multi-step scheme converge with a limited number of time steps (N_t).

In Figs. 2 and 3, the convergence behaviors of the non-dimensional results of the transient analyses of FG-GPLRC spherical panels with X-type distribution of the GPLs under blast loading against the DQ number of grid points along the r, and θ and ϕ directions are illustrated, respectively. The numerical stability and the fast convergence rate of results are observable. It can also be seen that five grid points in the radial direction (i.e, $N_r = 5$) and seven grid points along the two other directions (i.e, $N_\theta = N_\phi = 7$) are sufficient to obtain the acceptable results, respectively.

In order to verify the accuracy of the method, the transient thermoelastic responses of a FG hollow sphere in thermal environment subjected to a suddenly applied internal pressure are determined. Eslami et al. [63] analyzed this problem analytically. They assumed that the material properties of the FG sphere, except the Poisson's ratio, vary according to the following rule [63]

$$\chi = \chi_0 r^n \tag{34}$$

where χ_0 represents the corresponding material property at the outer FG shell surface and n is the non-homogeneity index. They used the following material properties, non-dimensional parameters and boundary conditions for the FG hollow sphere, respectively [63]

$$\nu = 0.3,\ E_0 = 200\ (\mathrm{GPa}), \alpha_0 = 1.2\times10^{-6}\left(\frac{1}{^{\circ}\mathrm{C}}\right);\ \hat{T} = \frac{T}{T(R_i)}, \hat{u} = \frac{u}{R_i}, \hat{\sigma}_{jj} = \frac{\sigma_{jj}}{\sigma_{rr}(R_i)} \text{ with } j = r,\theta;$$

$$T(R_i,t) = 10\ (^{\circ}\mathrm{C}),\ T(R_o,t) = 0\ (^{\circ}\mathrm{C}),\ \sigma_{rr}(R_i,t) = -50\ (\mathrm{MPa}),\ \sigma_{rr}(R_o,t) = 0 \quad \text{(35a-h)}$$

where ν , E_0 and α_0 are, respectively, the Poisson's ratio, Young's modulus and thermal expansion coefficient of sphere material. Also, T is the temperature at an arbitrary material point of the FG hollow sphere.

The non-dimensional temperature, radial displacement and stress components of both approaches are compared in Fig. 4. The results in this figure indicate close agreement between the present solution and the exact solution of Ref. [63] for different values of the non-homogeneity index (*n*).

As another comparative study, the free vibration of a truncated spherical shell with both edges clamped is investigated here. This example is adopted from the work of Qu et al. [64]. They employed an analytical method to solve formulation based on the FSDT. They considered the shell material properties as follows [64],

$$E = 168\ \mathrm{GPa},\ \nu = 0.3,\ \rho = 5700\ (\mathrm{kg/m}^3)$$

The first frequencies corresponding to the first six circumferential modes are tabulated with those obtained by Qu et al. [64] in Table 3. For the different values of the circumferential wave number (*m*), good agreement between the two approaches is quite obvious.

After demonstrating the computational efficiency and accuracy of the present approach, some parametric studies are carried out to investigate the transient behaviors of the multilayer FG-GPLRC spherical panels subjected to blast loading. To generate the numerical results, 400 time steps are used.

The effects of the GPLs distribution patterns on the time histories of the displacement and stress components of multilayer FG-GPLRC spherical panels under blast loading are illustrated in Fig. 5. As can be seen, the GPLs distribution patterns have important influences on the radial displacement and stress components of the FG-GPLRC spherical panels and their effects cannot be ignored. This figure indicates that the maximum radial displacements of the panels with O-type and V-type GPLs distribution patterns are almost the same and greater than those of the panels with uniform and X-type ones. However, the differences between the radial displacement components of the FG-GPLRC panels with different GPLs distribution patterns increase gradually with time. Based on the results in Fig. 5, a longer oscillatory response of the FG-GPLRC panels is noticed for the O-type GPLs distribution pattern, compared to other types of responses. Moreover, it is found that the largest stress components are belong to the FG-GPLRC panels with the O-type GPLs distribution pattern, which has the maximum radial displacement component too.

The effects of the GPLs weight fraction on the time histories of the non-dimensional field variables of FG-GPLRC spherical panels under blast loading are presented in Fig. 6. The FG-GPLRC panels with the X-type distribution of GPLs are analyzed in this example. The results show that adding a small amount of GPLs to the polymer matrix can significantly change the non-dimensional radial displacement and stress components of the FG-GPLRC spherical panels. Fig. 6 illustrates that for the different values of GPLs weight fraction, the differences of the radial displacements vary between 81% and 197%. The addition of GPLs to the matrix decreases the radial displacements of the panels, which indicates the increase of the overall panel stiffness. In addition, the transient stress components of the panels decrease with the increase of the W_{GPL} value. As can be expected, the period of oscillatory portions of the results decreases with the increase of the GPLs weight fraction.

In Fig. 7, the effects of the length-to-width ratio of GPLs on the transient responses of GPLRC spherical panels with O-distribution of GPLs are investigated. The results indicate that the effects of the length-to-width ratio of GPLs on the non-dimensional radial displacement and stress components of FG-GPLRC panels are not significant, especially at the beginning of impact loading. In contrast to the effects of the length-to-width ratio, the results in Fig. 8 show that the width-to-thickness ratio of GPLs has significant impact on the time histories of the non-dimensional mechanical field variables of the FG-GPLRC spherical panels. In this figure, the results of the FG-GPLRC spherical panels with the O-type GPLs distribution pattern and three different values of the width-to-thickness ratio of GPLs are compared. It is observed that by increasing the width-to-thickness ratio of GPLs, the non-dimensional radial displacement decreases. This suggests that the increase of the width-to-thickness ratio of the GPLs increases the stiffness of the FG-GPLRC panels. The increase in the panel stiffness is due to the fact that with the same amounts of GPLs, the load transfer will increase when larger surface contact areas between the GPLs and the polymer matrix are developed. Therefore, it can be concluded that the GPLs surface areas play an important role in improving the stiffness of the GPLRC panels; and with the same amounts of GPLs, those with larger surface areas are better reinforcement nanofillers than their counterparts with small surface areas.

Fig. 9 illustrates the effects of the opening angles (θ_0, ϕ_0) on the time histories of the results for the FG-GPLRC spherical panels with the V-type GPLs distribution pattern. The important impacts of these geometric parameters on the transient responses of the panels are evident. It can be easily realized that the increase of these angles decreases the overall stiffness of the FG-GPLRC panels. Consequently, and as proved by the presented results, the non-dimensional radial displacement of the structure must increase. Fig. 9 further demonstrates that the period of

oscillatory portions of the response increases with increasing θ_0 and ϕ_0. Moreover, the results reveal that increasing θ_0 and ϕ_0 leads to increases of the non-dimensional stress components of the FG-GPLRC spherical panels.

5. Conclusion

A three-dimensional numerical investigation of the dynamic responses of the multilayer FG-GPLRC spherical panels under blast loading was provided. The layerwise-differential quadrature method in combination with a non-uniform rational B-spline based multi-step time integration scheme was employed to discretize the motion equations. The convergence behavior and accuracy of the method were demonstrated. After that, the influences of the GPLs distribution patterns, GPLs weight fraction and dimension ratios, and the panel opening angles on the blast loading dynamic responses of the FG-GPLRC spherical panels were investigated. The results reveal that

1. The response time histories of the FG-GPLRC panels significantly depend on the GPLs distribution patterns.
2. The addition of a small amount of GPLs to polymer matrix can significantly enhance the stiffness of the resulting nanocomposites and reduce the time histories of the responses of the FG-GPLRC panels.
3. The GPLs distribution patterns have significant influences on the dynamic behaviors of FG-

   PLRC panels. For example, the X-type and uniform distributions of the GPLs provide the greatest stiffness, while the O-type and V-type GPLs distributions yield the minimum stiffness, respectively.

4. The increase of the width-to-thickness ratio of the GPLs increases the overall stiffness of the FG-GPLRC panels and consequently reduces the stress components generated by dynamic loading.
5. The increase of the GPLs width-to-thickness ratio decreases the period of oscillatory portions of the responses, whereas the GPLs length-to-width ratio has negligible influence on the time responses of the FG-GPLRC panel.
6. The increase of the opening angles reduces the overall panel stiffness of the FG-GPLRC panels, increases the period of oscillatory portions of the responses and increases the induced stress components generated by blast loading.

References

1. R. Atif, I. Shyha and F. Inam, Mechanical, thermal, and electrical properties of graphene-epoxy nanocomposites—a review, *Polymers* **8** (2016) 281.
2. D.G. Papageorgiou, I.A. Kinloch and R.J. Young, Mechanical properties of graphene and graphene-based nanocomposites, *Prog. Mater. Sci.* **90** (2017) 75–127.
3. J. Yang, H. Wu and S. Kitipornchai, Buckling and postbuckling of functionally graded multilayer graphene platelet-reinforced composite beams, *Compos. Struct.* **161** (2017) 111–8.
4. C. Feng, S. Kitipornchai and J. Yang, Nonlinear bending of polymer nanocomposite beams reinforced with non-uniformly distributed graphene platelets (GPLs), *Compos. B Eng*. **110** (2017) 132–140.
5. M. Song, S. Kitipornchai and J. Yang, Free and forced vibrations of functionally graded polymer composite plates reinforced with graphene nanoplatelets, *Compos. Struct*. **159** (2017) 579–588.

6. S. Zhao, Z. Zhao, Z. Yang, L. Ke, S. Kitipornchai and J. Yang, Functionally graded graphene reinforced composite structures: A review, *Eng. Struct*. **210** (2020) 110339.
7. S.K. Panda and B.N. Singh, Nonlinear free vibration of spherical shell panel using higher order shear deformation theory – A finite element approach, *Int. J. Pres. Ves. Pip*. **86**(6) (2009) 373-383.
8. S.H. Hosseini-Hashemi and M. Fadaee, On the free vibration of moderately thick spherical shell panel—A new exact closed-form procedure, *J. Sound Vib*. **330**(17) (2011) 4352-4367.
9. F. Tornabene, S. Brischetto, N. Fantuzzi and E. Viola, Numerical and exact models for free vibration analysis of cylindrical and spherical shell panels, *Compos. B Eng*. **81 (**2015) 231-250.
10. X. Xie, H. Zheng and G. Jin, Free vibration of four-parameter functionally graded spherical and parabolic shells of revolution with arbitrary boundary conditions, *Compos. B Eng.* **77** (2015) 59-73.
11. N. Fantuzzi, S. Brischetto, F. Tornabene and E. Viola, 2D and 3D shell models for the free vibration investigation of functionally graded cylindrical and spherical panels, *Compos. Struct.* **154** (2016) 573-590.
12. R. Mahapatra Trupti and K. Panda Subrata, Nonlinear free vibration analysis of laminated composite spherical shell panel under elevated hygrothermal environment: A micromechanical approach, *Aero Sci. Tec*. **49** (2016) 276-288.
13. A. Bryan, Free Vibration of Thin Spherical Shells, *J. Vib. Acoust*. **139**(6) (2017) 061020.
14. Y. Kiani, Free vibration of FG-CNT reinforced composite spherical shell panels using Gram-Schmidt shape functions, *Compos. Struct*. **159** (2017) 368-381.

15. Q. Wang, F. Pang, B. Qin and Q. Liang, A unified formulation for free vibration of functionally graded carbon nanotube reinforced composite spherical panels and shells of revolution with general elastic restraints by means of the Rayleigh–Ritz method, *Polymer Compos*. **39**(2) (2017) 924-944.
16. S.S. Atteshamuddin and M.G. Yuwaraj, Static and free vibration analysis of laminated composite and sandwich spherical shells using a generalized higher-order shell theory, *Compos. Struct*. **219** (2019) 129-146.
17. D.K. Biswal and S.C. Mohanty, Free vibration study of multilayer sandwich spherical shell panels with viscoelastic core and isotropic/laminated face layers, *Compos. B Eng*. **159** (2019) 72-85.
18. H. Li, F. Pang, X. Miao, S. Gao and F. Liu, A semi analytical method for free vibration analysis of composite laminated cylindrical and spherical shells with complex boundary conditions, *Thin Wall Struct*. **136** (2019) 200-220.
19. M. Shamloofard, A. Hosseinzadeh and MR. Movahhedy, Development of a shell superelement for large deformation and free vibration analysis of composite spherical shells, *Eng. Comput*. **37** (2021) 3551-3567.
20. Y. Du, L. Sun, S. Li and Y. Li, Vibration analysis of truncated spherical shells under various edge constraints, *Thin Wall Struct*. **147** (2020) 106544.
21. H. Zhou, P. Cong, X. Wang, T. Song, X. Huang, A dimensionless number for response of blast loaded steel plates, *Int. J. Struct. Stab. Dyn*. **21**(5) (2021) 2150072.
22. J. Rennie, S. Kaewunruen, C. Baniotopoulos, Nonlinear blast responses of thin shell roof over long span structures, *Int. J. Struct. Stab. Dyn*. **21**(3) (2021) 2150031.

23. P. Fuzhen, L. Haichao, C. Hailong and S. Yanhe, Free vibration analysis of combined composite laminated cylindrical and spherical shells with arbitrary boundary conditions, *Mech. Adv. Mate. Struct*. **28**(2) (2021) 182-199.

24. M. Subramani, M. Ramamoorthy, A.B. Arumugam, R. Selvaraj, Free and forced vibration characteristics of CNT reinforced composite spherical sandwich shell panels with MR elastomer core, *Int. J. Struct. Stab. Dyn.* **21**(10) (2021) 2150136.

25. K. Foroutan, H. Ahmadi, Nonlinear static and dynamic buckling analysis of imperfect stiffened double-layer FGP shallow spherical shells embedded within elastic foundations, *Int. J. Struct. Stab. Dyn.* **13**(6) (2021) 2150070.

26. J. Gong, Q. Wang, B. Nie, Z. Ge, Experimental study on ground vibration caused by the blast loading of an explosion vessel, *Int. J. Struct. Stab. Dyn.* **22**(1) (2022) 2250003.

27. D. Liu, J. Sun and L. Lan, Elasticity Solutions for in-plane free vibration of FG-GPLRC circular arches with various end conditions, *Appl. Sci.* **10** (2020) 4695.

28. A. Chaikittiratana and N. Wattanasakulpong, Gram-Schmidt-Ritz method for dynamic response of FG-GPLRC beams under multiple moving loads, *Mech. Based Des. Struc*. (2020).

29. S.Z. Tabatabaei-Nejhad, P. Malekzadeh and M. Eghtesad, Out-of-plane vibration of laminated FG-GPLRC curved beams with piezoelectric layers, *Thin Wall Struct*. **150** (2020) 106678.

30. F. Bahranifard, M.R. Golbahar Haghighi and P. Malekzadeh, In-plane responses of multilayer FG-GPLRC curved beams in thermal environment under moving load, *Acta Mechanica* **231** (2020) 2676-2696.

31. M. Habibi, M. Safarpour and H. Safarpour, Vibrational characteristics of a FG-GPLRC viscoelastic thick annular plate using fourth-order Runge-Kutta and GDQ methods, *Mech. Based Des. Struc.* (2020).

32. Y. Wang, R. Zeng and M. Safarpour, Vibration analysis of FG-GPLRC annular plate in a thermal environment, *Mech. Based Des. Struc*. (2020).

33. R. Ansari, R. Hassani and J. Torabi, Mixed-type formulation of higher-order shear deformation theory for vibration and buckling analysis of FG-GPLRC plates using VDQFEM, *Compos. Struct*. **235** (2020) 111738.

34. Y. Dong, Y. Li, D. Chen and J. Yang, Vibration characteristics of functionally graded graphene reinforced porous nanocomposite cylindrical shells with spinning motion, *Compos. B Eng*. **145** (2018) 1-13.

35. S.M. Hosseini and C. Zhang, Coupled thermoelastic analysis of an FG multilayer graphene platelets-reinforced nanocomposite cylinder using meshless GFD method: A modified micromechanical model, *Eng. Anal. Bound. Elem*. **88** (2018) 80-92.

36. Y.H. Dong, B. Zhu, Y. Wang, L.W. He, Y.H. Li and J. Yang, Analytical prediction of the impact response of graphene reinforced spinning cylindrical shells under axial and thermal loads, *Appl. Math. Model* **71** (2019) 331-348.

37. Y. Heydarpour, M. Mohammadzaheri, M. Ghodsi, P. Soltani, F. AlJahwari, I. Bahadur and B. Al-Amri, Application of the hybrid DQ-Heaviside-NURBS method for dynamic analysis of FG-GPLRC cylindrical shells subjected to impulse load, *Thin-Walled Struct*. **155** (2020) 106914.

38. A. Eyvazian, T.A. Sebaey, K.K. Żur, A. Khan, H. Zhang and S.H.F. Wong, On the dynamics of FG-GPLRC sandwich cylinders based on an unconstrained higher-order theory, *Compos. Struct.* **267** (2021) 113879.

39. Y. Heydarpour, P. Malekzadeh, R. Dimitri and F. Tornabene, Thermoelastic analysis of rotating multilayer FG-GPLRC truncated conical based on a coupled TDQM-NURBS scheme, *Compos. Struct*. **235** (2019) 111707.

40. T.D. Singha, M. Rout, T. Bandyopadhyay and A. Karmakar, Free vibration of rotating pretwisted FG-GRC sandwich conical shells in thermal environment using HSDT, *Compos. Struct*. **257** (2021) 113144.

41. Y. Heydarpour, P. Malekzadeh and F. Gholipour, Thermoelastic analysis of FG-GPLRC spherical shells under thermo-mechanical loadings based on Lord-Shulman theory, *Compos. B Eng*. **164** (2019) 400-424.

42. A. Eyvazian, F. Musharavati, P. Talebizadehsardari and T.A. Sebaey, Free vibration of FG-GPLRC spherical shell on two parameter elastic foundation, *Steel Compos. Struct*. **36**(6) (2020) 711–727.

43. V.N.V. Do and C.H. Lee, Static bending and free vibration analysis of multilayered composite cylindrical and spherical panels reinforced with graphene platelets by using isogeometric analysis method, *Eng. Struct*. **215** (2020) 110682.

44. D. Liu, Y. Zhou and J. Zhu, On the free vibration and bending analysis of functionally graded nanocomposite spherical shells reinforced with graphene nanoplatelets: Three-dimensional elasticity solutions, *Eng. Struct*. **226** (2021) 111376.

45. A. Wang, H. Chen, Y. Hao and W. Zhang, Vibration and bending behavior of functionally graded nanocomposite doubly-curved shallow shells reinforced by graphene nanoplatelets, *Results Phys*, **9** (2018) 550-559.

46. A. Bidzard, P. Malekzadeh and S.R. Mohebpour, Vibration of multilayer FG-GPLRC toroidal panels with elastically restrained against rotation edges, *Thin Wall. Struct*. **143** (2019) 106209.

47. A. Wang, H. Chen and W. Zhang, Nonlinear transient response of doubly curved shallow shells reinforced with graphene nanoplatelets subjected to blast loads considering thermal effects, *Compos, Struct*, **225** (2019) 111063.

48. A. Bidzard, P. Malekzadeh and S.R. Mohebpour, Influences of pressure and thermal environment on nonlinear vibration characteristics of multilayer FG-GPLRC toroidal panels on nonlinear elastic foundation, *Compos. Struct*. **259** (2021) 113503.

49. N.K. Akhmedov, A.H. Sofiyev, Asymptotic analysis of three-dimensional problem of elasticity theory for radially inhomogeneous transversally-isotropic thin hollow spheres, *Thin Wall. Struct.* **139** (2019) 232-241.

50. M. Avey, E. Yusufoglu, On the solution of large-amplitude vibration of carbon nanotube-based double-curved shallow shells. *Math. Meth. Appl. Sci.* (2020) 1-13.

51. A.H. Sofiyev, M. Avey, N.K uruoglu, An approach to the solution of nonlinear forced vibration problem of structural systems reinforced with advanced materials in the presence of viscous damping. *Mech. Syst. Signal Process.* **161** (2021) 107991.

52. M. Avey, N. Fantuzzi, A.H. Sofiyev, N. Kuruoglu, Nonlinear vibration of multilayer shell-type structural elements with double curvature consisting of CNT patterned layers within different theories, *Compos. Struct.* **275** (2021) 114401.

53. G.L. She, H.B. Liu, B. Karami, Resonance analysis of composite curved microbeams reinforced with grapheme nanoplatelets, *Thin Wall. Struct.* **160** (2021) 107407.

54. Y.Y. Zhang, Y.X. Wang, X. Zhang, H.M. Shen, G.L. She, On snap-buckling of FG-CNTR curved nanobeams considering surface effects", *Steel Compos. Struct.* **38(3)** (2021) 293-304.

55. L. Lu, G.L. She, X. Guo, Size-dependent postbuckling analysis of graphene reinforced composite microtubes with geometrical imperfection, *Int. J. Mech. Sci*. **199** (2021) 106428.

56. Y. Heydarpour, P. Malekzadeh, Dynamic stability of rotating FG-CNTRC cylindrical shells under combined static and periodic axial loads, *Int. J. Struct. Stab. Dyn.* **18**(12) (2018) 1850151.

57. G. Zhang, C. Xiao, A. Rahimi, M. Safarpour, Thermal and mechanical buckling and vibration analysis of FG-GPLRC annular plate using higher order shear deformation theory and generalized differential quadrature method, *Int. J. Struct. Stab. Dyn.* **12**(2) (2020) 2050019.

58. C. Wang, R. Liu, J. Huang, Geometrically nonlinear dynamic response of perforated plates by modified differential quadrature method, *Int. J. Struct. Stab. Dyn.* **21**(7) (2021) 2150097.

59. Y. Heydarpour and M.M. Aghdam, Response of VSCL plates under moving load using a mixed integral-differential quadrature and novel NURBS based multi-step method, *Compos. B Eng*. **140** (2018) 260-280.

60. Y. Heydarpour and M.M. Aghdam, A new multi-step technique based on the non-uniform rational basis spline curves for non-linear transient heat transfer analysis of functionally graded truncated cone, *Heat Transfer Eng*. **40** (2019) 588-603.

61. Y.H. Dong, B. Zhu, Y. Wang, L.W. He, Y.H. L and J. Yang, Analytical prediction of the impact response of graphene reinforced spinning cylindrical shells under axial and thermal loads, *Appl. Math. Model* **71** (2019) 331-348.

62. A.A. Khdeir and J.N. Reddy, Exact solutions for the transient response of symmetric cross-ply laminates using a higher-order plate theory, *Compos. Sci. Technol*. **34** (1989) 205–224.

63. M.R. Eslami, M.H. Babaei and R. Poultangari, Thermal and mechanical stresses in a functionally graded thick sphere, *Int. J. Pres. Ves. Pip*. **82** (2005) 522–527.

64. Q. Yegao, L. Xinhua, Y. Guoqing, M. Guang, A unified formulation for vibration analysis of functionally graded shells of revolution with arbitrary boundary conditions, *Compos. B Eng.* **50** (2013) 381–402.

Table 1. Material properties of the epoxy and GPLs [37].

Material	Epoxy	GPLs
E (GPa)	3	1010
ν	0.34	0.186
$\rho\left(\text{kg/m}^3\right)$	1200	1062.5

Table 2. Comparison between the obtained results of U-GPLRC spherical panels using NURBS based multi-step technique and the Newmark's scheme $\left[W_{GPL}=1\%,\ \xi=\eta=\mu=0.5,,\theta_0=\phi_0=60^{\circ},\right.$ $\left.N_r=5,\ N_\theta=N_\phi=7,P_0=100(\text{MPa}),\ t=0.003(\text{s})\right]$.

	NURBS-based scheme		Newmark's scheme	
N_t	U	CPU time (s)	U	CPU time (s)
10	1.5037	0.002034	0.7009	5.703471
20	0.8371	0.032786	0.9254	13.095610
50	0.9516	0.036091	0.9584	19.031749
100	0.9673	0.047834	0.9738	37.882056
150	0.9725	0.059034	0.9762	53.385991
200	0.9763	0.067201	0.9771	81.044821
300	0.9775	0.103871	0.9774	134.39031
400	0.9779	0.229106	0.9774	273.80063

Table 3. Accuracy of the frequency parameters $\lambda_{m1}\ \left[=\omega_{m1}R\sqrt{\rho\left(1-\nu^2\right)\ /E}\right]$ for a clamped truncated spherical shell $\left(h/R=0.05,\ \varphi_0=\pi/8,\right.$ $\left.\varphi_1=\pi/2\right)$.

m	Present	Qu et al. [64]
0	0.9789	0.98710
1	1.0143	1.02639
2	0.9969	1.00292
3	0.9851	0.99803
4	1.0254	1.04274
5	1.0948	1.12623
6	1.2095	1.24578

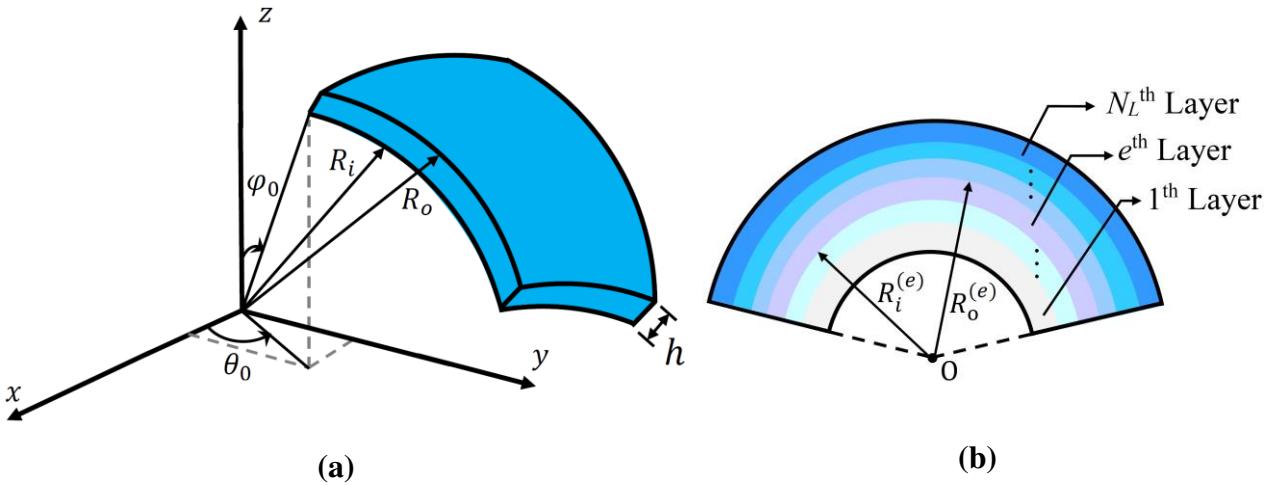

Fig. 1: The geometry of multilayer FG-GPLRC spherical panels.

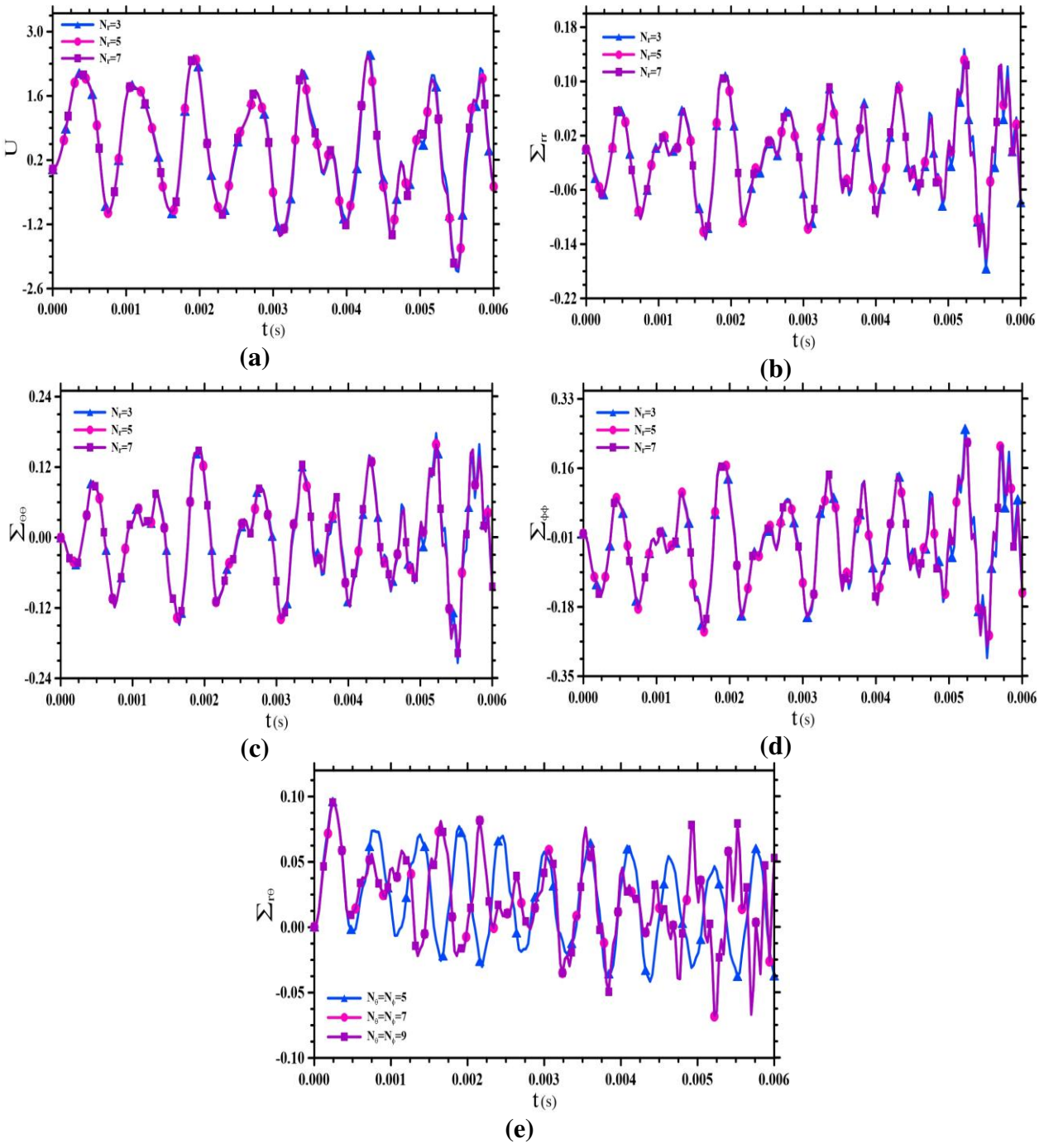

Figs. 2 (a)-(e): Convergence of the dynamic field variables along the radial direction for the clamped X-GPLRC spherical panels $\left[W_{GPL}=1\%,\quad \xi=\eta=\mu=0.5,\quad ,\quad \theta_0=\phi_0=60^{\circ}\quad ,\quad N_\theta=N_\phi=7\,,P_0=100\,(\mathrm{MPa})\right]$.

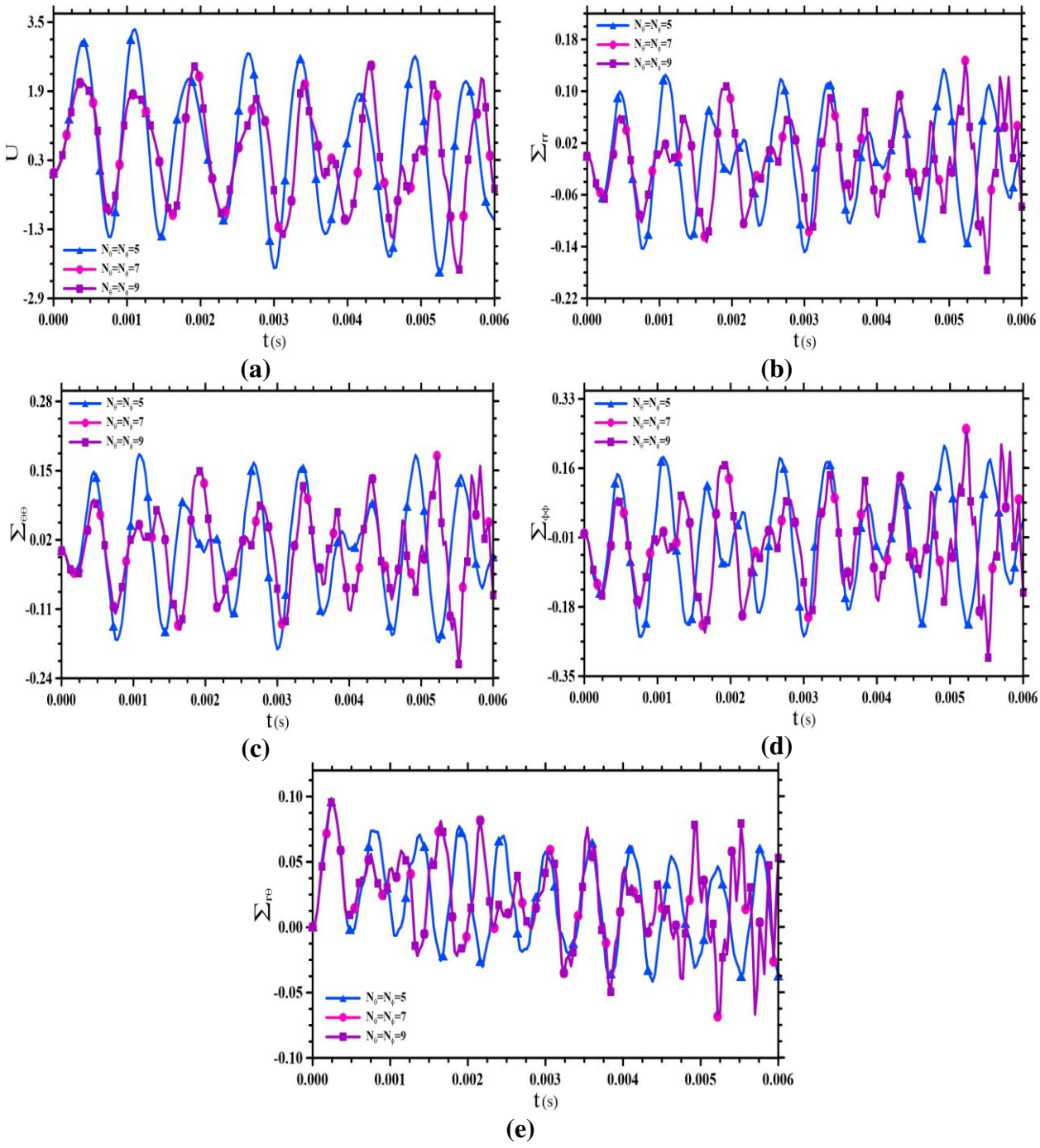

Figs. 3 (a)-(e): Convergence of the dynamic field variables along the θ and ϕ directions for the clamped X-GPLRC spherical panels $\left[W_{GPL}=1\%,\quad \xi=\eta=\mu=0.5,\quad ,\quad \theta_0=\phi_0=60^{\circ}\quad ,\right.$ $\left.N_r=5\,, F_{\circ}=0.2,\ P_0=100\,(\mathrm{MPa})\right]$.

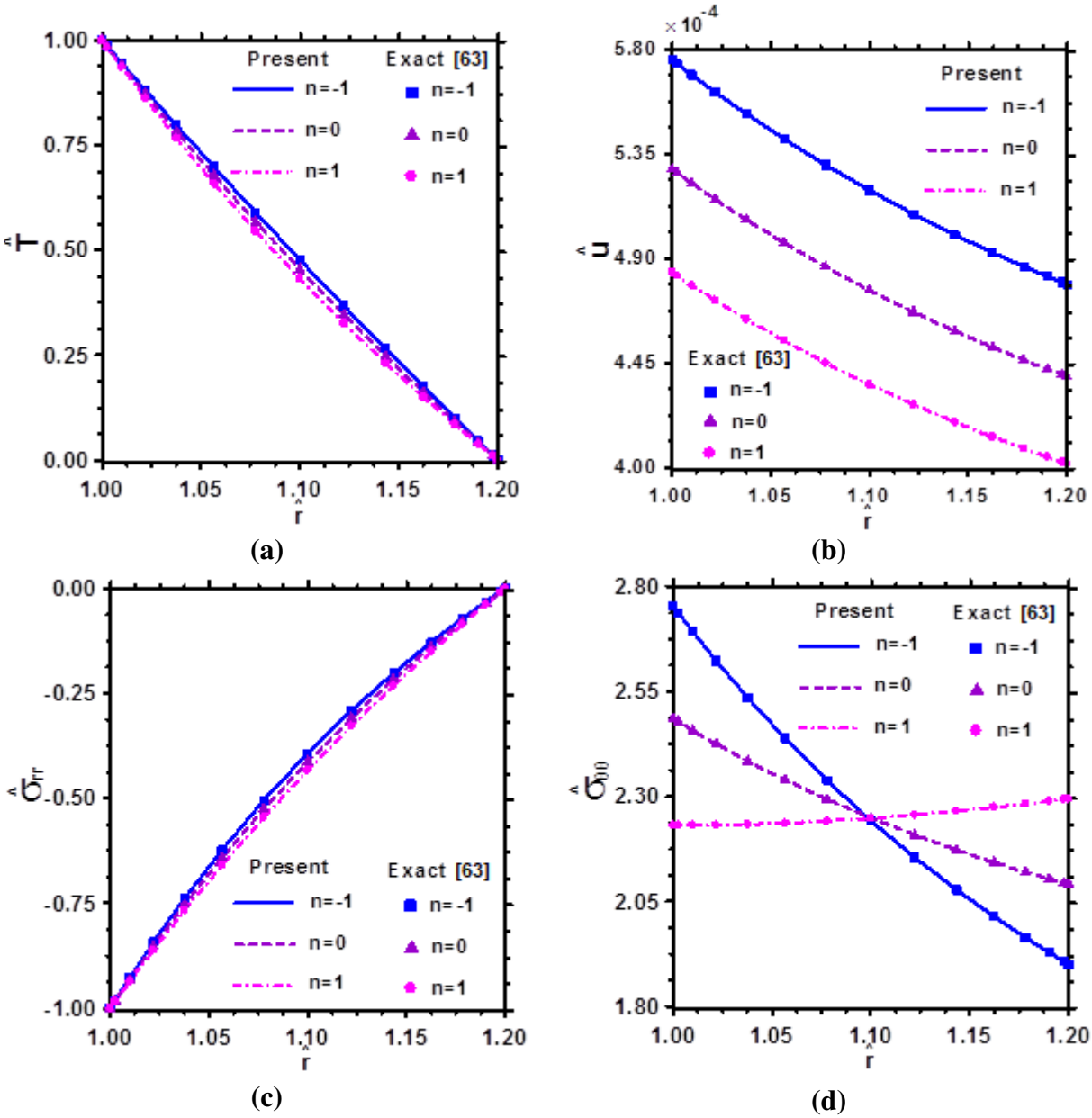

Figs. 4 (a)-(d): Comparison of results across the thickness of a FG hollow sphere subjected to internal pressure in thermal environment $\left[R_{\mathrm{i}}=1(\mathrm{m}),\ R_{\mathrm{o}}=1.2(\mathrm{m})\right]$.

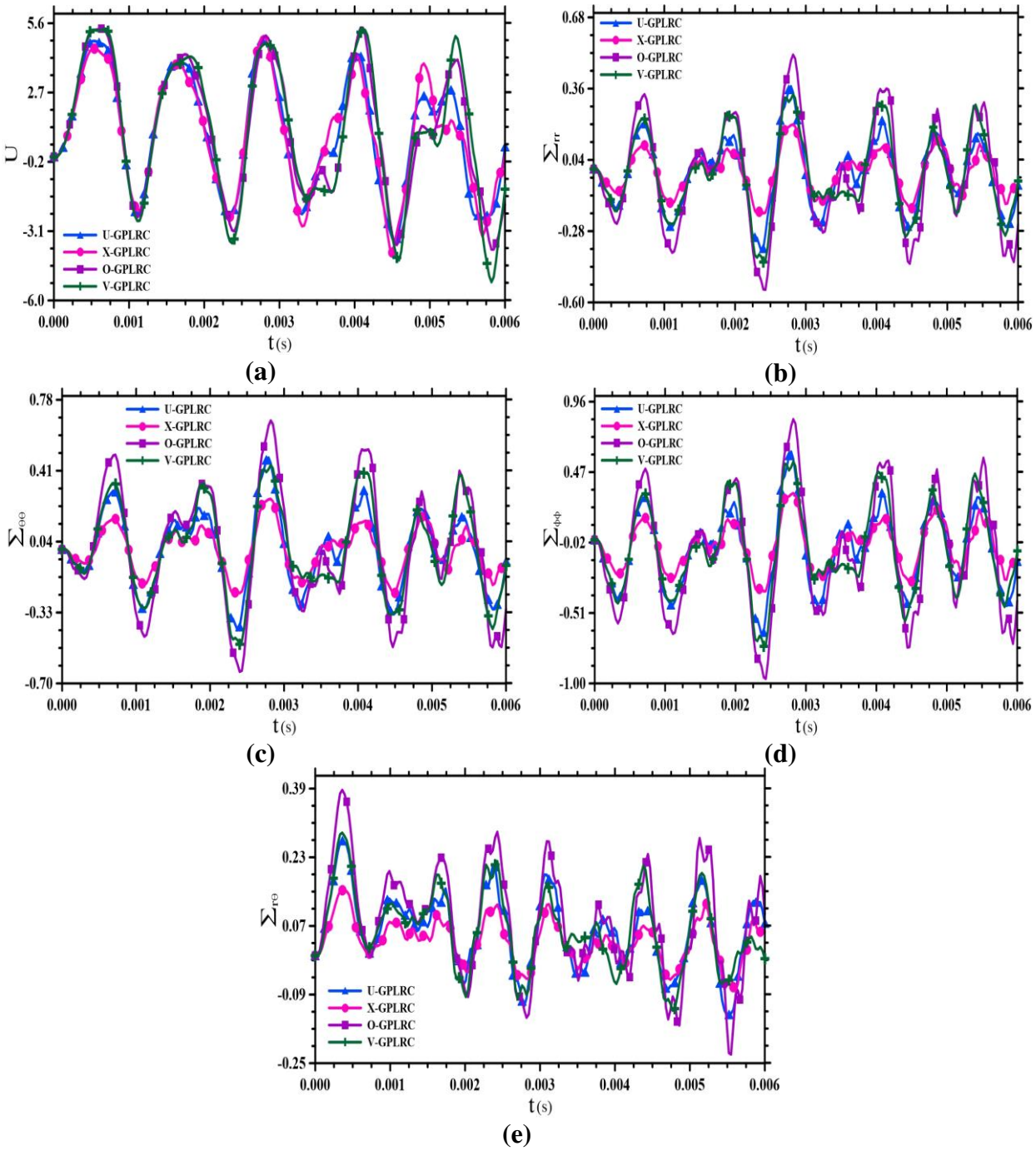

Figs. 5 (a)-(e): The effects of GPLs distribution pattern on the time histories of the results for FG-GPLRC clamped spherical panels $\left[W_{GPL}=0.3\%,\ \ \xi=\eta=\mu=0.5,\ \ ,\ \ \theta_0=\phi_0=60^{\circ}\ \ ,\ \ N_\theta=N_\phi=7\,,\ N_r=5\,,\ P_0=50\,(\mathrm{MPa})\right]$.

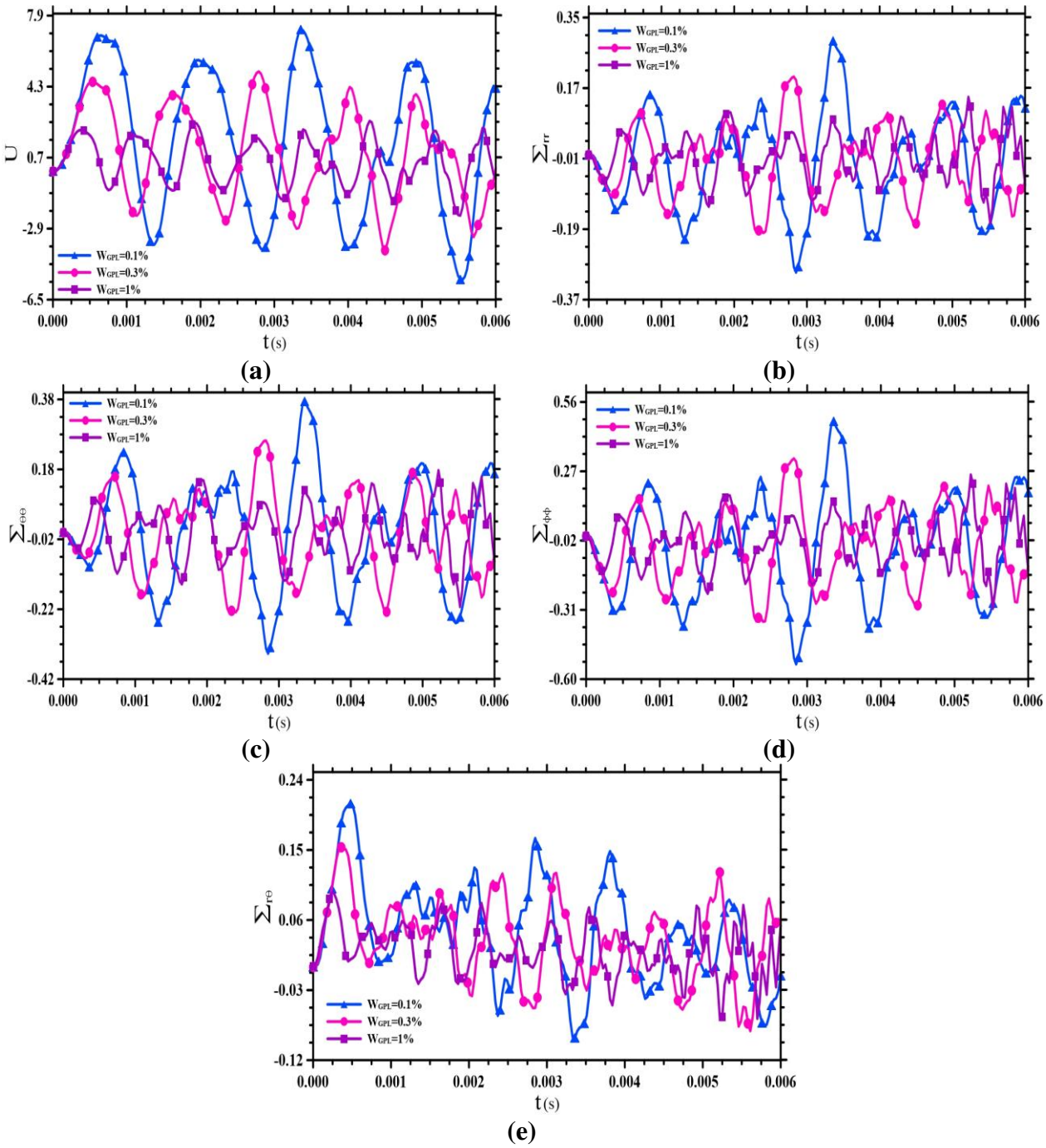

Figs. 6 (a)-(e): The effects of GPLs weight fraction on the time histories of the results for the FG-GPLRC clamped spherical panels with the X-type GPLs distribution pattern $\left[\xi=\eta=\mu=0.5,,\theta_0=\phi_0=60^{\circ},\ N_\theta=N_\phi=7,\ N_r=5,\ P_0=100\,(\mathrm{MPa})\right]$.

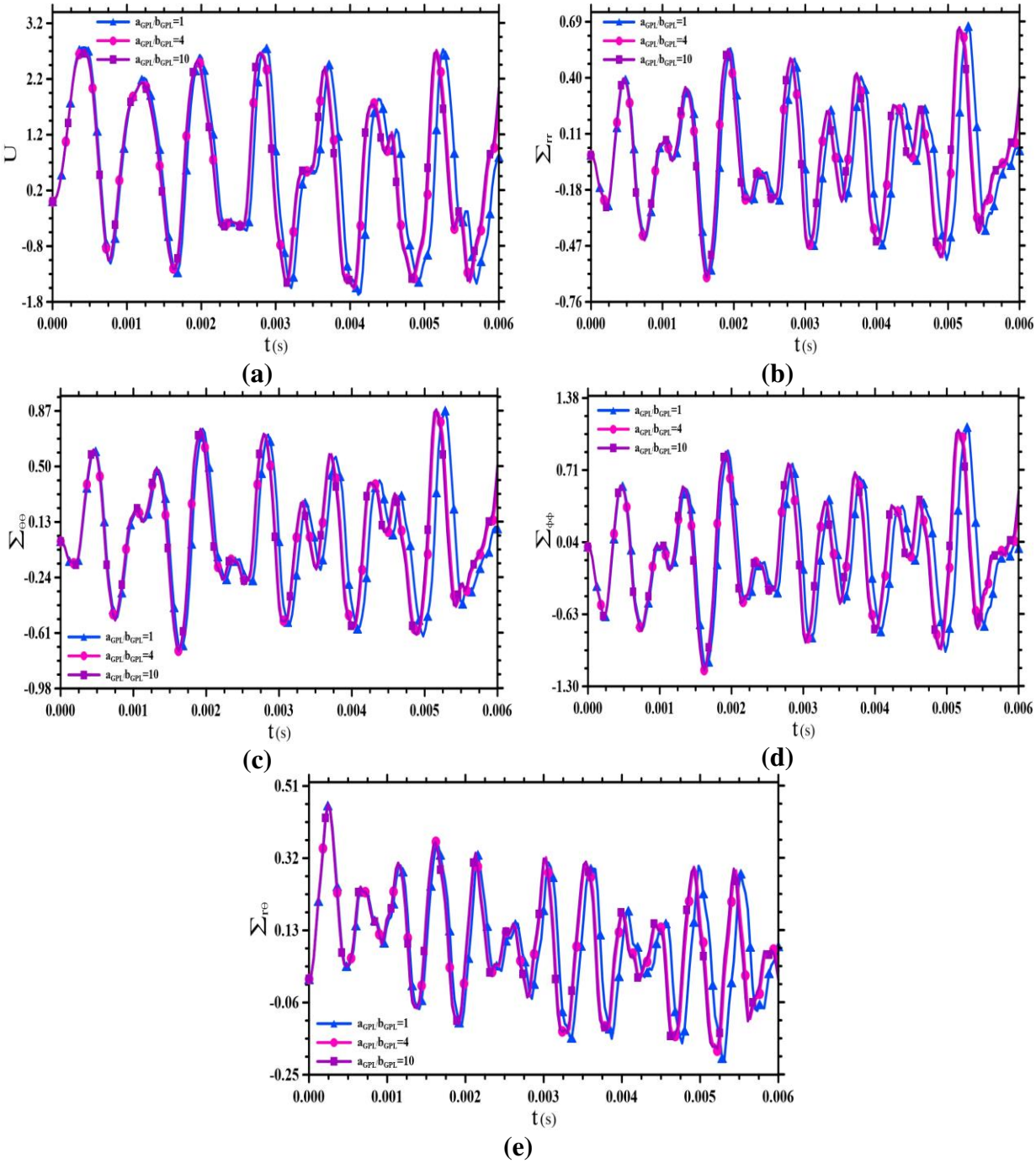

Figs. 7 (a)-(e): The effects of length-to-width thickness ratio of GPLs on the on the time histories of the dynamic field variables of the O-GPLRC clamped spherical panels with O-type GPLs distribution pattern $\left[W_{GPL}=1\%,\ \xi=\eta=\mu=0.5,\ ,\ \theta_0=\phi_0=60^{\circ}\ ,\ N_\theta=N_\phi=7\ ,\ N_r=5\ ,\ P_0=100(\mathrm{MPa})\right]$.

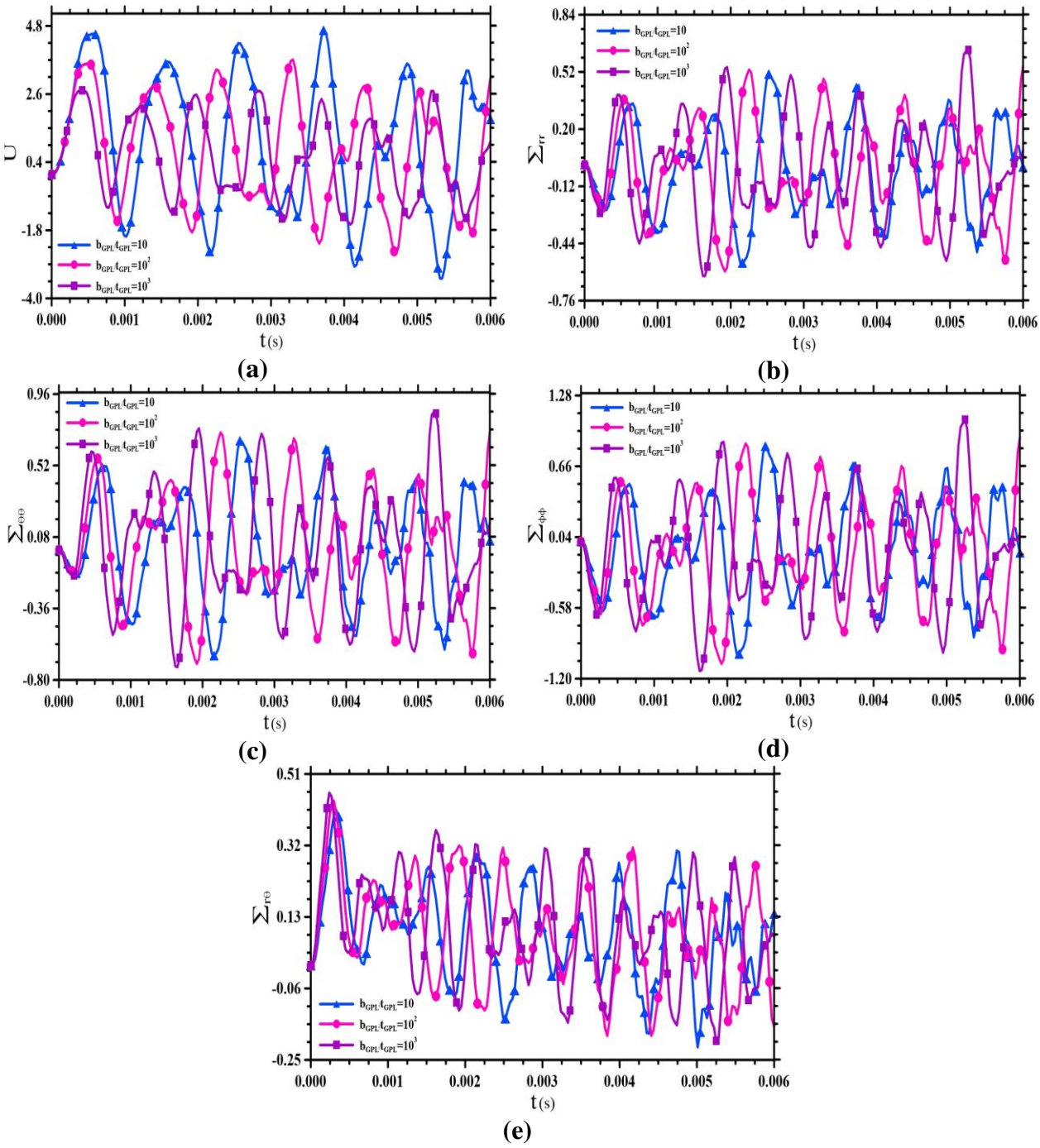

Figs. 8 (a)-(e): The effects of width-to-thickness ratios of GPLs on the time histories of the dynamic field variables of the O-GPLRC clamped spherical panels $\left[W_{GPL}=1\%,\ \xi=\eta=\mu=0.5,,\theta_0=\phi_0=60^{\circ},\ N_\theta=N_\phi=7,\ N_r=5,\ P_0=100\,(\mathrm{MPa})\right]$.

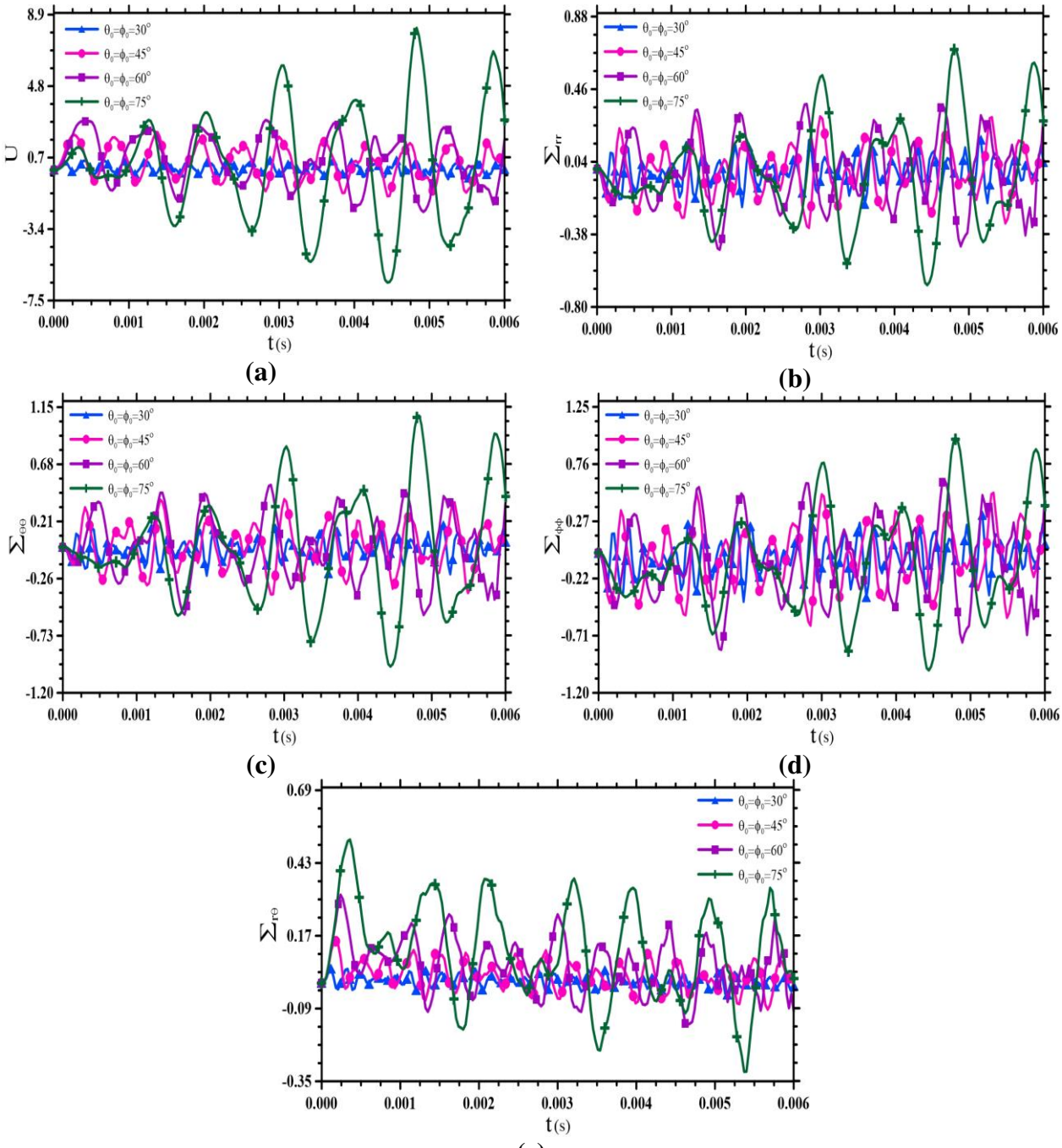

Figs. 9 (a)-(d): The effect of opening angles (θ_0, ϕ_0) on the time histories of the results for the FG-GPLRC spherical panels with V-type GPLs distribution pattern $[W_{GPL} = 1\%,\ \xi = \eta = \mu = 0.5,\ N_\theta = N_\phi = 7,\ N_r = 5,\ P_0 = 100\,(\text{MPa})]$.